

Non-Negligible Imaginary Part of the Spin-Mixing Conductance and its Impact on Magnetization Dynamics in Heavy-Metal–Ferromagnet Bilayers

Janusz Dubowik,^{1,*} Piotr Graczyk,¹ Adam Krysztofik^{ID},¹ Hubert Główinski,¹ Emerson Coy^{ID},² Karol Załęski^{ID},² and Iwona Gościańska¹

¹*Institute of Molecular Physics, Polish Academy of Sciences, ul. Smoluchowskiego 17, 60-179 Poznań, Poland*

²*NanoBioMedical Centre, Adam Mickiewicz University, ul. Wszechnicy Piastowskiej 3, 61-614 Poznań, Poland*



(Received 10 June 2019; revised manuscript received 9 March 2020; accepted 2 April 2020; published 5 May 2020)

In this paper we present experimental verification of the magnitude of the imaginary part of the spin-mixing conductance in bilayers comprising heavy metals. We present results of broadband ferromagnetic resonance studies on heterostructures consisting of Finemet ($\text{Fe}_{66.5}\text{Cu}_1\text{Nb}_3\text{Si}_{13.5}\text{B}_6\text{Al}_7$) thin films covered by Pt and Ta wedge layers with the aim of observing spin-pumping effects and evaluating both the real ($\text{Re}[g_{\text{eff}}^{\uparrow\downarrow}]$) and imaginary ($\text{Im}[g_{\text{eff}}^{\uparrow\downarrow}]$) parts of the spin-mixing conductance. In particular, we show that the imaginary part of the spin-mixing conductance cannot be regarded as negligible, and we discuss its influence on magnetization dynamics. For Finemet/Ta bilayers, the ratio $\text{Re}[g_{\text{eff}}^{\uparrow\downarrow}]/\text{Im}[g_{\text{eff}}^{\uparrow\downarrow}] = 0.38$; that is, the fieldlike torque dominates over the dampinglike torque in such a system. The experimental results are analyzed in the framework of a recent microscopic theory that allows us to estimate the value of the interfacial spin-orbit interaction and confirm its important role. The role of material and interface parameters is also discussed.

DOI: 10.1103/PhysRevApplied.13.054011

I. INTRODUCTION

Increasing demand for data storage has intensively driven research efforts to find new memory technologies in the past decades. One currently developed approach for magnetization switching employs the spin-orbit torque (SOT) exerted in a heavy-metal–ferromagnet system [1–4]. In comparison to the formerly proposed spin-transfer-torque–based magnetic random-access memories (MRAMs), use of the SOT allows us to decouple a read path from a write current path in a memory cell, offering several advantages: simultaneous read and write operations that shorten memory access time [5]; independent optimization of both current paths; and increased cell endurance previously delimited with the aging of a thin tunnel barrier [6,7].

Originating from the bulk spin Hall effect and/or the interfacial Rashba-Edelstein effect [8,9], the spin-orbit torque arises from a nonequilibrium spin accumulation at the bilayer interface, and can be decomposed into two components: a dampinglike torque and a fieldlike torque. Much scientific effort has been devoted to recognizing key parameters characterizing heavy-metal–ferromagnet bilayers that ensure the most efficient switching [6,10,11]. One such parameter is the spin Hall angle, defined as a

conversion efficiency between charge currents and pure spin currents [12,13]. In terms of the magnitude of the spin current transferred into the ferromagnetic layer, transparency of the bilayer interface, which is described by the so-called spin-mixing conductance [14], plays an equally important role. Moreover, for current-induced spin-orbit torques, it has been shown that the real part of the spin-mixing conductance contributes to the dampinglike torque, while the imaginary part contributes to the fieldlike torque [15]. The significance of the latter torque is the focus of this paper.

In the context of spin torque, the total spin torque related to transport across an interface is given by $\text{Re}[g_{\uparrow\downarrow}]\vec{m} \times (\vec{\mu} \times \vec{m}) + \text{Im}[g_{\uparrow\downarrow}]\vec{\mu} \times \vec{m}$, i.e., the sum of the dampinglike (longitudinal) and fieldlike (transverse) torques, respectively. Here $\vec{\mu}$ is the spin accumulation. While the dampinglike torque is ascribed to the absorption of the transverse spin angular momentum, the fieldlike torque is due to the reflection or its incomplete absorption [16].

Spin-mixing conductance is usually determined using spin-torque ferromagnetic resonance [17]. An alternative method involves the use of the reciprocal effect, i.e., spin pumping, commonly detected using vector network analyzer ferromagnetic resonance (VNA-FMR) measurements [18,19]. While the enhancement of magnetization precession damping due to spin pumping has been extensively studied, enabling the evaluation of the real part of the spin-mixing conductance [20–28], the imaginary

*dubowik@ifpan.poznan.pl

part has been either discarded [29] or predicted to be small in the drift-diffusion model [30,31]. In particular, the ratio between the real and imaginary parts of the spin-mixing conductance roughly determines the ratio between the dampinglike and fieldlike components of the spin Hall torques [31], which is of the order of 10^1 . Interestingly, the interfacial Rashba torque shows mostly a fieldlike character and, hence, the ratio of the dampinglike to fieldlike torques can be reversed [31].

From among a few reports discussing the changes of the resonance field (or a “fieldlike” torque) in the context of spin-pumping effects, it is worth listing a few in which either a field shift or $\text{Im}[g_{\text{eff}}^{\uparrow\downarrow}]$ have been mentioned. In the ferromagnetic resonance (FMR) experiments of Mizukami *et al.* [22], apparent changes in the gyromagnetic ratio (corresponding to $\text{Im}[g_{\text{eff}}^{\uparrow\downarrow}]$) were observed experimentally, without comprehensive explanation. By analyzing spin-orbit torques and spin pumping in Ni-Fe/Pt bilayers, Nan *et al.* [32] estimated that $\text{Re}[g_{\text{eff}}^{\uparrow\downarrow}] = 2.2 \times 10^{15} \text{ cm}^{-2}$ is only 3.7 times larger than $\text{Im}[g_{\text{eff}}^{\uparrow\downarrow}] = 0.6 \times 10^{15} \text{ cm}^{-2}$. They also demonstrated that the spin-orbit dampinglike and fieldlike torques scale with the interfacial spin current transmission. Sun *et al.* [33] found that a strong damping enhancement in yttrium iron garnet/Pt bilayers is accompanied by a substantial shift in the resonance field. They concluded that the spin-pumping effects may originate partially from ferromagnetic ordering due to the magnetic proximity effect in Pt atomic layers near the interface. However, they have not linked the resonance field shift with $\text{Im}[g_{\text{eff}}^{\uparrow\downarrow}]$. An elegant interpretation of the imaginary part of the spin-mixing conductance generated by ferromagnetic (FM) insulators with exchange-coupled local moments at the interface to a nonmagnetic metal has recently been proposed by Cahaya *et al.* [34]. They assumed that a coherent motion of the proximity Ruderman-Kittel-Kasuya-Yosida (RKKY) spin density (e.g., in Pt) is locked to the precessing magnetization of the local moments, leading to a renormalization of the effective magnetic field. Moreover, the recently discovered spin Hall magnetoresistance [35] offered a unique possibility to measure $\text{Im}[g_{\text{eff}}^{\uparrow\downarrow}]$ for the interface of a normal metal in contact with a magnetic insulator by exposing it to out-of-plane magnetic fields. However, the applied model itself was based on the assumption that $\text{Re}[g_{\text{eff}}^{\uparrow\downarrow}]/\text{Im}[g_{\text{eff}}^{\uparrow\downarrow}] \gg 1$ [36,37].

It is also important to point out that the fieldlike torque has recently received considerable attention since experimental results concerning spin currents in Ta/Co₄₀Fe₄₀B₂₀/MgO suggest that it may play a decisive role in governing magnetization dynamics, although the values of $\text{Im}[g_{\text{eff}}^{\uparrow\downarrow}]$ have not been determined from the requisite measurements [38]. Furthermore, it was shown that the domain wall reflection at sample edges of such heterostructure relies on the fieldlike torque that is crucial in

the deterministic SOT switching mechanism [27]. In this work we study spin pumping and spin current transport in Finemet films covered by platinum (Pt) and tantalum (Ta) with a strong emphasis on the role of the imaginary part of the spin-mixing conductance.

II. MICROSCOPIC ANALYSIS OF SPIN PUMPING

Recently, consistent analysis of spin pumping has been presented by Tatara and Mizukami [39] for both metallic and insulating ferromagnets. Let us summarize the main results of their analysis. In the scattering approach, the spin current pumped by FMR results in modification of the Gilbert damping parameter α and the gyromagnetic ratio γ_0 of a lone FM film via spin-mixing conductance [40,41]:

$$\tilde{\alpha} = \alpha_0 + \frac{a^3}{4\pi S d_F} \text{Re}[g_{\text{eff}}^{\uparrow\downarrow}] \quad (1)$$

and

$$\tilde{\gamma} = \gamma_0 \left(1 - \frac{a^3}{4\pi S d_F} \text{Im}[g_{\text{eff}}^{\uparrow\downarrow}] \right)^{-1}. \quad (2)$$

Here a is the lattice constant, S is the magnitude of the localized spin, and d_F is the thickness of the ferromagnet. As $a^3/4\pi S = \hbar\gamma_0/4\pi M_S$ and $\gamma_0 = g_0\mu_B/\hbar$, where M_S is the saturation magnetization, \hbar is the reduced Planck constant, and μ_B is the Bohr magneton, Eqs. (1) and (2) can be rewritten as

$$\delta\alpha = \tilde{\alpha} - \alpha_0 = \frac{g_0\mu_B}{4\pi M_S d_F} \text{Re}[g_{\text{eff}}^{\uparrow\downarrow}] \quad (3)$$

and

$$\frac{\delta g}{g_0} = \frac{\tilde{g} - g_0}{g_0} \cong \frac{g_0\mu_B}{4\pi M_S d_F} \text{Im}[g_{\text{eff}}^{\uparrow\downarrow}]. \quad (4)$$

Hence,

$$\frac{\delta\alpha}{\delta g/g_0} \cong \frac{\text{Re}[g_{\text{eff}}^{\uparrow\downarrow}]}{\text{Im}[g_{\text{eff}}^{\uparrow\downarrow}]}, \quad (5)$$

and the ratio of $\text{Re}[g_{\text{eff}}^{\uparrow\downarrow}]$ to $\text{Im}[g_{\text{eff}}^{\uparrow\downarrow}]$ can be easily estimated from the spin-pumping experiments. Note that the same relation with respect to $\text{Re}[g_{\text{eff}}^{\uparrow\downarrow}]/\text{Im}[g_{\text{eff}}^{\uparrow\downarrow}]$ has been assumed for the ratio of the dampinglike and fieldlike components of the spin Hall torque [31].

In the microscopic analysis, the magnetization dynamics are derived by evaluating the spin accumulation in a nonmagnetic metal as a result of interface hopping. One of the main consequences of the analysis [39] is an approximation of enhancement of the Gilbert damping parameter,

i.e.,

$$\delta\alpha = \eta \frac{a}{d_F} \frac{1}{\epsilon_F^2} \tilde{t}_\uparrow^0 \tilde{t}_\downarrow^0, \quad (6)$$

where ϵ_F is the Fermi energy and η is a dimensionless coefficient roughly equal to 1 (see the Supplemental Material [42]). The so-called hopping amplitudes, \tilde{t}_\uparrow^0 and \tilde{t}_\downarrow^0 , correspond to the energy required for an electron to hop between orbitals at a ferromagnetic-nonmagnetic interface in the absence of the spin-orbit interaction. Similarly, the change in the g factor due to spin pumping can be rewritten, using Eq. (84) of Ref. [39], as

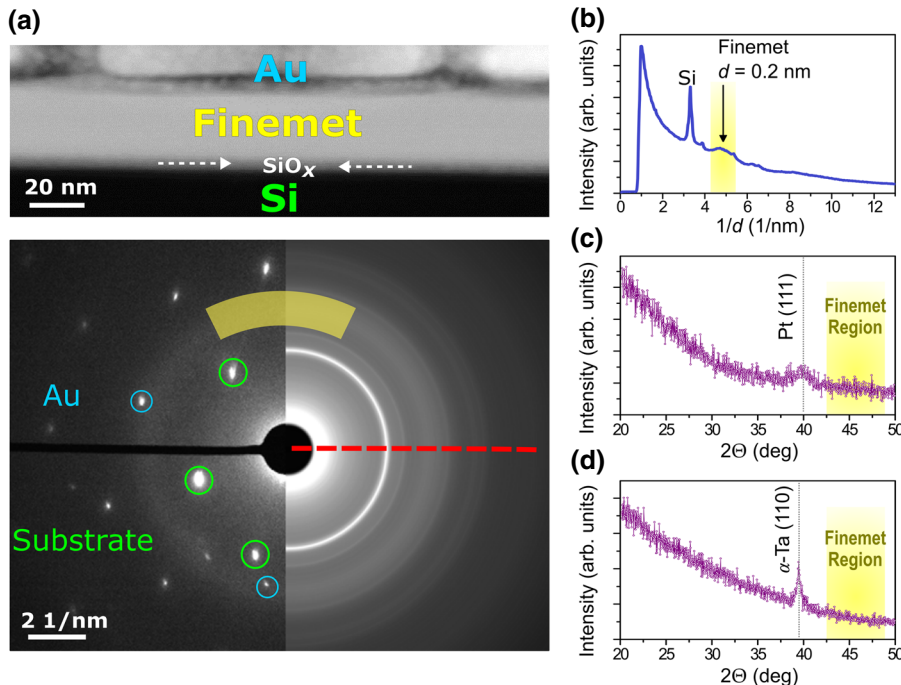
$$\frac{\delta g}{g_0} = \eta \frac{a}{d_F} \frac{1}{\epsilon_F^2} \tilde{\gamma}_{xz} (\tilde{t}_\uparrow^0 + \tilde{t}_\downarrow^0), \quad (7)$$

where $\tilde{\gamma}_{xz}$ represents the interface spin-orbit interaction having a unit of energy. Equation (7) suggests that a high value of $\delta g/g_0$ is expected if a strong interface spin-orbit interaction exists. Therefore, the ratio $\delta\alpha/(\delta g/g_0)$, which is directly accessible experimentally, becomes

$$\frac{\delta\alpha}{\delta g/g_0} = \frac{\tilde{t}_\uparrow^0 \tilde{t}_\downarrow^0}{\tilde{\gamma}_{xz} (\tilde{t}_\uparrow^0 + \tilde{t}_\downarrow^0)}. \quad (8)$$

III. SAMPLES STRUCTURE AND METHODS

To verify and experimentally examine the main results of the quoted theory, we fabricate F/NM bilayers using Fe_{66.5}Cu₁Nb₃Si_{13.5}B₆Al₇ (Finemet, F) as the ferromagnetic layer and Pt, Ta as a nonmagnetic metal (NM).



Instead of commonly employed Permalloy films, we extensively use Finemet for the following reasons: (i) exceptional smoothness of Finemet surfaces [43]; (ii) a low Gilbert damping parameter, smaller in comparison to Permalloy [44–46]; and (iii) a relatively small inhomogeneous linewidth ΔH_0 of 3–6 Oe, indicating a low density of defects [43]. The Finemet films with different thicknesses are deposited at room temperature by pulsed laser deposition (base pressure of 8×10^{-8} mbar) on naturally oxidized Si substrates and covered *in situ* with wedge-shaped capping layers of Pt or Ta ($0 < d_{NM} < 7$ nm) using radio frequency magnetron sputtering. The nominal thicknesses of Finemet, $d_F = 10, 15, 20, 30, 40$ nm for the Pt cover layer and $d_F = 2, 3.5, 5, 10$ nm for the Ta cover layer, are confirmed with x-ray reflectivity measurements, while thickness profiles of the NM capping layer are additionally verified using the energy dispersive spectroscopy in a scanning electron microscope. Atomic-force-microscopy measurements of the Finemet surface yielded rms roughness of 0.1 nm.

To determine the structural properties of the films, we conduct HRTEM experiments and grazing incident x-ray diffraction (GiXRD). In the selected area electron diffraction (SAED) pattern of Fig. 1(a) we show a diffuse ring marked in yellow, indicating the occurrence of a nanocrystalline phase in the Finemet film. Apart from substrate peaks, reflections corresponding to a gold layer are visible, with which the Finemet film is coated before the preparation of a cross section by the focused ion beam. The nanocrystalline band corresponds roughly to the interplanar distance of 0.2 ± 0.1 nm [see Fig. 1(b)], which is extracted via rotational averaging using the DiffTools

FIG. 1. (a) Low-magnification scanning electron image of a Finemet control layer (25 nm) coated ex-situ with Au for cross-section preparation, and the corresponding SAED pattern, including both the substrate and the Au covering film (bottom panel). The dashed red line shows the direction of the profile taken from the rotational averaging, displayed in (b). The profile image shows the clear position of Finemet ($d = 0.2$ nm) plus the highly intense Si peaks. Finally, (c) and (d) show the GiXRD spectra of Finemet(30 nm)/Pt(6 nm) and Finemet(10 nm)/Ta(6 nm), respectively, where the textures of Pt(111) and α -Ta(110) covering layers can be seen.

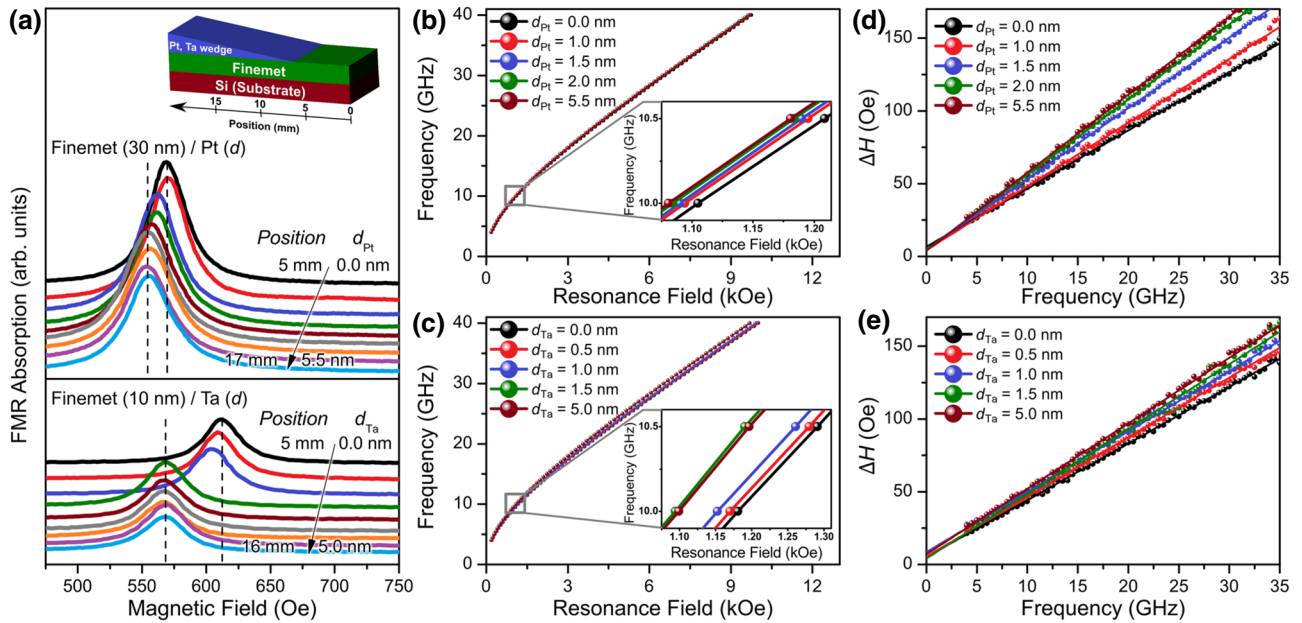


FIG. 2. Exemplary VNA-FMR measurement results for a 30-nm-thick Finemet film covered with Pt and a 10-nm-thick Finemet film covered with Ta. (a) Typical FMR spectra taken at $f = 7$ GHz for various positions along the wedge-shaped Pt and Ta layers. The inset schematically shows the wedge structure. In (b) and (c), the frequency versus resonance field dependencies fitted using Eq. (9) are shown. The insets show enlarged regions near $f = 10$ GHz. In (d) and (e) the linewidth versus frequency dependencies fitted using Eq. (10) are presented.

plugin for DigitalMicrographTM [47]. This result is congruent with the simulation of a Finemet unit cell (using the CaRInE Crystallography software, Lattice 2.8), yielding $d_{(110)} = 0.1980$ nm. However, the highest intensity reflection (110), expected to be at 45.75 angle 2Θ , is not observed in the grazing incident x-ray diffraction, as marked by the shaded areas in Figs. 1(c) and 1(d). Nevertheless, these measurements allowed us to determine the structure of capping Pt and Ta layers. We conclude that the studied bilayer systems consist of nanocrystalline Finemet films covered with α -Ta (i.e., bcc) or Pt with well-defined (110) and (111) textures, respectively.

Ferromagnetic resonance measurements of the samples are carried out at room temperature on a coplanar waveguide (CPW) in the in-plane configuration over a frequency range of 4–40 GHz, as detailed in Refs. [48] and [49]. For each thickness d_{NM} , we measure the field swept complex transmission parameter $S_{21}(H)$ by placing the sample at a certain position along the wedge [see Fig. 2(a)]. The real and imaginary transmission spectra are fitted using the Lorentzian and anti-Lorentzian functions in a similar way to that described in Ref. [50]. From the fits, the resonance field H_r and resonance linewidth ΔH (full width at half maximum) are evaluated at several frequencies f . In short, our method involves the use of a single sample with a fixed thickness d_F wherein the capping layer is wedge shaped so, by scanning the sample over the central line of a CPW, we can determine parameters of magnetization dynamics as a

function of d_{NM} . Such an approach is of crucial importance because it eliminates the problem of the proper choice of a reference layer [51]. Since deposition conditions (and consequently film properties) may differ slightly in each sputtering or ablation process, we set the beginning of the NM wedge 6–7 mm from the substrate's edge, allowing for the measurements of a lone Finemet film in every F/NM bilayer [see the inset of Fig. 2(a)]. To theoretically model the magnetization dynamics, we follow the methodology presented in Refs. [52–56]. Using the finite-element method in COMSOL Multiphysics®, the Landau-Lifshitz equation with spin-torque term is numerically solved in the framework of the diffusive model. Detailed information on the utilized formalism can be found in the Supplemental Material [42].

IV. EXPERIMENTAL RESULTS

Typical resonance spectra of Finemet(30 nm)/Pt(0–5 nm) and Finemet(10 nm)/Ta(0–5 nm) samples, measured at $f = 7$ GHz for various positions along the wedge, are displayed in Fig. 2(a). It can be seen that an increase in linewidth is also accompanied by a substantial, yet unexpected, shift in the resonance field H_r as the Pt thickness increases. The shift is negative (i.e., towards lower fields) and indicates systematic changes in the gyromagnetic ratio or the effective magnetization. To obtain values of the g factor, we perform fittings of f versus H_r dependencies

rather than evaluate changes in H_r measured at one fixed frequency so as not to make an additional assumption about the effective magnetization value M_{eff} . As shown in Figs. 2(b) and 2(c), the relation follows Kittel's dispersion $f = (g\mu_B/h)\sqrt{H_r(H_r + 4\pi M_{\text{eff}})}$; however, detailed analysis of the fitting residuals reveals that Finemet films possess a non-negligible anisotropy field H_a (see the Supplemental Material [42]). Hence, the model is extended to

$$f = \frac{g\mu_B}{h} \sqrt{(H_r + H_a)(H_r + H_a + 4\pi M_{\text{eff}})}. \quad (9)$$

It should be emphasized that the inclusion of H_a in Eq. (9) (along with the g factor and M_{eff}) results in three coupled adjustable parameters that are not orthogonal to each other during the least-squares nonlinear fitting process [57]. Therefore, we follow the methodology presented in Ref. [57] and applied an asymptotic analysis (presented below) to the data obtained over a finite range of frequencies to precisely determine the value of the g factor. Across the set of samples, we find that the Finemet films are characterized by H_a in the range 7 ± 2 Oe.

The Gilbert damping parameter α and the inhomogeneous broadening ΔH_0 for a given d_F and different thicknesses d_{NM} are obtained from linear fits to the resonance linewidth ΔH as a function of frequency, according to the standard expression [58]

$$\Delta H(f) = \frac{4\pi\alpha}{\gamma} f + \Delta H_0. \quad (10)$$

Even for relatively thick Finemet films [e.g., 30 nm as in Fig. 2(d)], it is clearly seen that the slopes of the $\Delta H(f)$ dependencies experience a substantial change with increasing thickness of Pt. Indeed, as summarized in Fig. 3(a), a continuous increase in the damping parameter α is observed for each investigated bilayer.

The damping of a lone Finemet film is equal to $\alpha = (5.8 \pm 0.3) \times 10^{-3}$, although for the thinnest layer in the set with Pt [10 nm; see Fig. 3(a)] it is slightly elevated to the value of $\alpha = (7.80 \pm 0.07) \times 10^{-3}$ [59]. A similar increase is observed in the set of samples with Ta [see Fig. 3(b)]. The ΔH_0 parameter remains below 10 Oe, with the mean value of 6.4 Oe indicating a low density of surface defects and, therefore, negligible extrinsic contributions to the linewidth, such as two-magnon scattering [see the insets of Figs. 3(a) and 3(b)]. However, values of ΔH_0 for 2-nm-thick Finemet [see the inset of Fig. 3(b)] reach 100 Oe and may originate from substrate roughness, making such contribution observable in an ultrathin-film regime. Using the equation describing the damping enhancement due to spin pumping [60],

$$\alpha = \alpha_0 + \frac{g\mu_B}{4\pi M_S} \frac{\text{Re}[g_{\text{eff}}^{\uparrow\downarrow}]}{d_F} \left[1 - \exp\left(-\frac{2d_{\text{NM}}}{\lambda_{\text{SF}}}\right) \right], \quad (11)$$

we obtain the real part of the spin-mixing conductance, $\text{Re}[g_{\text{eff}}^{\uparrow\downarrow}] = (3.14 \pm 0.23) \times 10^{15} \text{ cm}^{-2}$, and, additionally, the spin-diffusion length, $\lambda_{\text{SF}} = 2.8 \pm 0.5$ nm, for bilayers with Pt.

To determine the imaginary part of $g_{\text{eff}}^{\uparrow\downarrow}$, an analysis of the g factor is performed according to Eq. (4). First, the influence of a finite fitting range on the obtained value of the g factor is examined. As shown in Fig. 3(c), with the increasing fitting range specified by the upper frequency f_{up} , the statistical error of the g factor decreases and the value begins to saturate when plotted as a function of f_{up} . Note that the error bars in Fig. 3(c) correspond to approximately 0.1% of the value at 30 GHz and approximately 0.04% for 40 GHz. It is claimed that, for large enough resonance fields, the fitted g -factor value becomes independent of a fitting range and can therefore be extrapolated from the $g_{\text{fit}}(1/f_{\text{up}}^2)$ dependence [57]. Although this claim is not verifiable, since every FMR spectrometer is limited by either available fields or frequencies, it should be highlighted that, in terms of the analysis provided herein, the method allows us to reasonably determine the difference between g -factor values of the uncovered Finemet films and those capped with the nonmagnetic metal. As can be seen in Figs. 3(d)–3(f), the difference $\delta g = \tilde{g} - g_0$ is essentially equivalent whether it is evaluated for $f_{\text{up}} = 40$ GHz or for $f_{\text{up}} \rightarrow \infty$ ($1/f_{\text{up}}^2 \rightarrow 0$). However, by taking the asymptotic values of \tilde{g} and g_0 into account, we provide better statistical accuracy for such subtle changes in the g factor when investigating relatively thick magnetic films. The observed mild oscillations in g_{fit} found at the high-frequency region originate from the small in-plane anisotropy field and random white noise, as described in Ref. [57]. For a platinum thickness of 1.5 nm [depicted by a red line in Fig. 3(d)], it even allows for the observation of an intermediate value of the g factor that falls between \tilde{g} and g_0 , which is difficult to conclude when the fitting is performed merely up to 40 GHz. This suggests that, with the appearance of a nonmagnetic layer, the enhancement in the g factor does not occur in an immediate, steplike way but follows a gradual increase until saturated. As presented in Figs. 3(d) and 3(e), the asymptotically fitted g factor for $d_{\text{Pt}} > 4$ nm already converges to nearly the same value \tilde{g} . Moreover, the obtained difference δg is greater for the thinner Finemet film, following the theoretical prediction given by Eq. (4). For the 20-nm-thick Finemet covered with Pt, $\delta g = (5.1 \pm 0.4) \times 10^{-3}$, while for the 10-nm-thick layer, $\delta g = (6.7 \pm 0.4) \times 10^{-3}$. Such a result provides clear evidence of a spin-pumping influence on magnetization dynamics expressed by the imaginary part of the spin-mixing conductance. Following this observation, it is expected that the difference δg will be larger for even thinner films. For the set of samples with Ta deposited on 2–10-nm-thick Finemet, this influence is indeed much more pronounced; see Fig. 4. Also, a

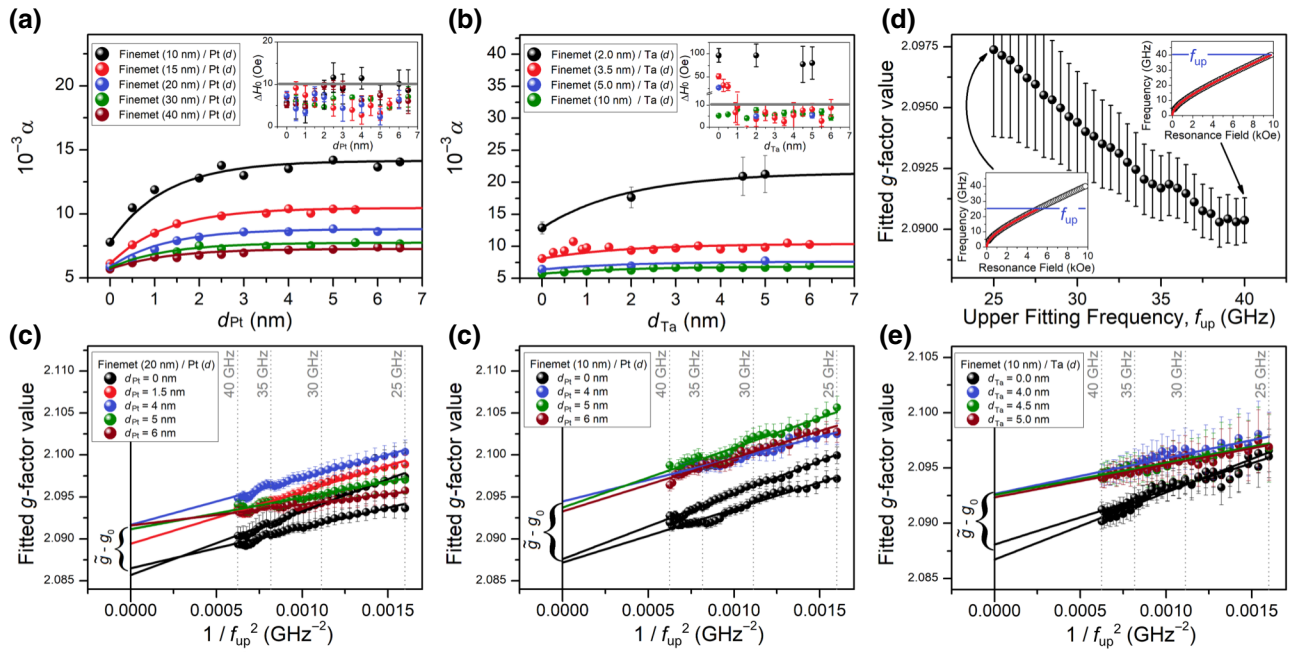


FIG. 3. (a),(b) The Gilbert damping parameter α as a function of the Pt and Ta film thicknesses. The solid lines are obtained by simultaneous fit to all collected data using Eq. (11). The insets show the values of the ΔH_0 parameter. (c) g -factor values for a 20-nm-thick Finemet film fitted using Eq. (9) for different frequency ranges defined by f_{up} as shown in the insets. In (d) and (e) fitted values of the g factor are plotted as a function of f_{up}^{-2} for 20-nm- and 10-nm-thick Finemet films, respectively, with different Pt thicknesses d_{Pt} . In (f) fitted values of the g factor are plotted as a function of f_{up}^{-2} for a 10-nm-thick Finemet film with different Ta thicknesses d_{Ta} . Double sets of data for $d_{\text{Pt,Ta}} = 0$ nm (black symbols and lines) derive from measurements of the lone Finemet film taken at different positions outside the Pt or Ta wedge.

quasilinear enhancement in the g factor is observed as the thickness of Ta increases from 0 to 2 nm.

The main experimental results of this paper are juxtaposed in Fig. 5, where $\delta\alpha$ and $\delta g/g_0$ are plotted against

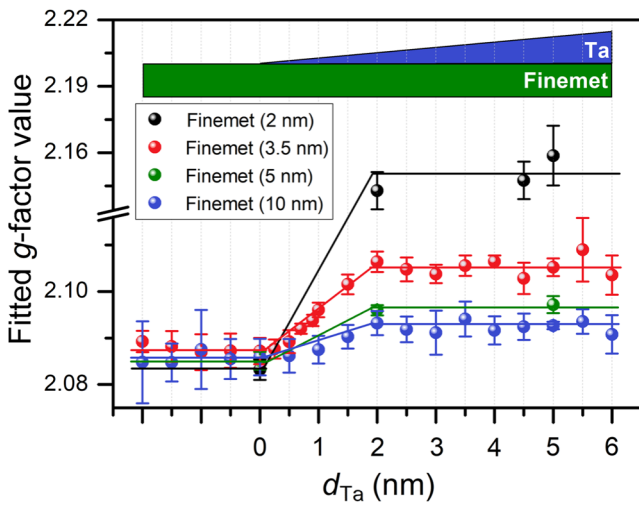


FIG. 4. Dependence of the g factor on a Ta layer thickness for Finemet/Ta bilayers with $d_F = 2$ – 10 nm. The continuous lines serve as visual guides.

the inverse thickness d_F for Finemet/Pt and Finemet/Ta bilayers. The real and imaginary parts of the spin-mixing conductance are determined from the slopes of linear fits according to Eqs. (3) and (4). For the sample covered with platinum, $\text{Re}[g_{\text{eff}}^{\uparrow\downarrow}] = (3.05 \pm 0.14) \times 10^{15} \text{ cm}^{-2}$, in agreement with the value obtained above from a simultaneous fit to the data presented in Fig. 3(a). We obtain $\text{Im}[g_{\text{eff}}^{\uparrow\downarrow}] = (1.69 \pm 0.22) \times 10^{15} \text{ cm}^{-2}$; therefore, the ratio $\text{Re}[g_{\text{eff}}^{\uparrow\downarrow}]/\text{Im}[g_{\text{eff}}^{\uparrow\downarrow}] = 1.81$, implying that the imaginary part of the spin-mixing conductance cannot in general be regarded as negligible, in contrast to many common views [17,29,39]. A strikingly different relation is observed for the Finemet film covered by tantalum. As can be seen from Fig. 5(b), the slope of $\delta g/g_0$ is substantially higher than the slope of $\delta\alpha$ vs d_F^{-1} . Here $\text{Re}[g_{\text{eff}}^{\uparrow\downarrow}] = (0.61 \pm 0.05) \times 10^{15} \text{ cm}^{-2}$ and $\text{Im}[g_{\text{eff}}^{\uparrow\downarrow}] = (1.61 \pm 0.07) \times 10^{15} \text{ cm}^{-2}$; hence, the ratio $\text{Re}[g_{\text{eff}}^{\uparrow\downarrow}]/\text{Im}[g_{\text{eff}}^{\uparrow\downarrow}] = 0.38$. It should be emphasized at this point that, for the 2-nm-thick Finemet film ($1/d_F = 0.5 \text{ nm}^{-1}$), the value of $\delta g/g_0$ significantly deviates from the linear relationship. We find that in such a thin film the saturation magnetization decreases to $450 \pm 34 \text{ emu/cm}^3$ (possibly due to variations in Finemet's complex composition [45]), resulting in the augmented value of $\delta g/g_0$

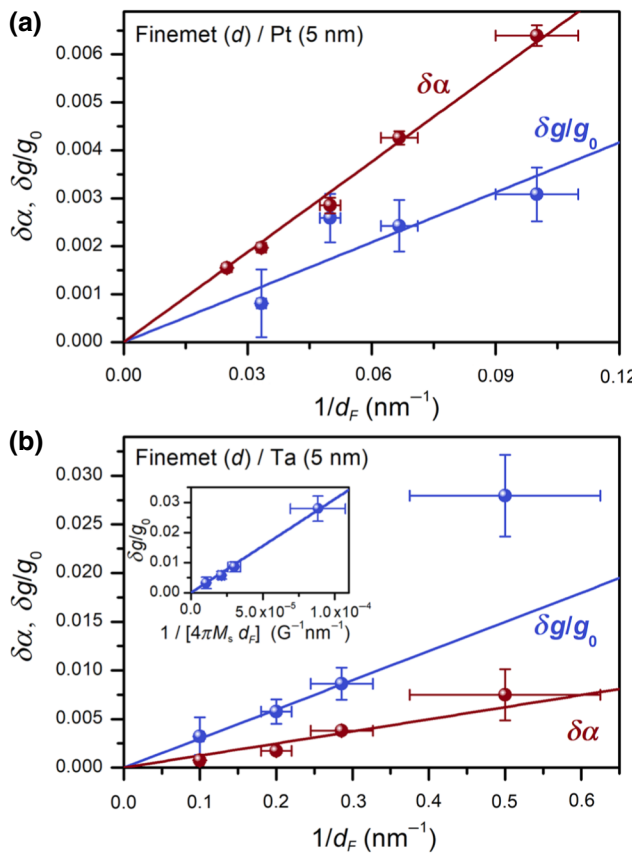


FIG. 5. Gilbert damping enhancement and relative change in the g factor due to spin pumping for (a) Finemet/Pt and (b) Finemet/Ta bilayers. The solid lines are fits to the data according to Eqs. (3) and (4). The inset in (b) shows that $\delta g/g_0$ scales almost perfectly with $(4\pi M_s d_F)^{-1}$ if the magnetization of the film experiences serious changes with d_F [see Eq. (4)].

[see Eq. (4)]. Therefore, to determine $\text{Im}[g_{\text{eff}}^{\uparrow\downarrow}]$, the fitting is performed to a $\delta g/g_0$ vs $(4\pi M_s d_F)^{-1}$ dependence, as shown in the inset of Fig. 5(b).

V. DISCUSSION

A. Comparison of experimental results with other studies

For Finemet/Pt bilayers, our results nearly agree with those obtained by Mizukami *et al.* [22]. Keeping in mind that they had two interfaces (Pt/Permalloy/Pt), their study yielded $\text{Re}[g_{\text{eff}}^{\uparrow\downarrow}]$ and $\text{Im}[g_{\text{eff}}^{\uparrow\downarrow}]$ equal to $3 \times 10^{15} \text{ cm}^{-2}$ and $0.6 \times 10^{15} \text{ cm}^{-2}$, respectively. For Finemet/Ta bilayers, the impact of the Ta layer on damping is significantly reduced compared to Pt, in agreement with former studies [22–24]. The estimated real part of the spin-mixing conductance, $\text{Re}[g_{\text{eff}}^{\uparrow\downarrow}] = 0.61 \times 10^{15} \text{ cm}^{-2}$, coincides with earlier reports for Permalloy/Ta ($0.51 \times 10^{15} \text{ cm}^{-2}$) [22], Co₂MnGe/Ta ($0.55 \times 10^{15} \text{ cm}^{-2}$) [23], and Co₄₀Fe₄₀B₂₀/Ta ($0.54\text{--}1 \times 10^{15} \text{ cm}^{-2}$) [24,61]

bilayers, confirming that the weak damping enhancement for Ta arises from a small value of $\text{Re}[g_{\text{eff}}^{\uparrow\downarrow}]$ [25,62]. Therefore, F/Ta bilayers highlight the interesting property that spin pumping has a minor effect on α , in accordance with Ref. [63].

In contrast, the results for the imaginary part of the spin-mixing conductance for Finemet/Ta bilayers show different behavior from that observed by Mizukami *et al.* [22] for Permalloy/Ta structures. The impact of Ta on the g factor results in a rather high value of $\text{Im}[g_{\text{eff}}^{\uparrow\downarrow}] = 1.61 \times 10^{15} \text{ cm}^{-2}$. Their observations concerning the g factor versus d_{Py} are not confirmed by our measurements. Instead of a substantial down shift in the g factor corresponding to $\text{Im}[g_{\text{eff}}^{\uparrow\downarrow}] = -0.46 \times 10^{15} \text{ cm}^{-2}$ (inferred from only one experimental point for a thin Permalloy film of 3 nm; see Fig. 6 of Ref. [22]), we see in Fig. 5 a regular behavior that can be nicely fitted using Eq. (4). From Fig. 4 we can further confirm that the increase in the g value for F/Ta bilayers is regular and saturates for $d_{\text{Ta}} > 2 \text{ nm}$. As we show in Sec. V, the impact of a considerable value of $\text{Im}[g_{\text{eff}}^{\uparrow\downarrow}]$ on spin transport in Ta may have important consequences in the magnetization dynamics.

For Finemet/Pt bilayers, $\delta\alpha/\delta g/g_0$ (or, equivalently, $\text{Re}[g_{\text{eff}}^{\uparrow\downarrow}]/\text{Im}[g_{\text{eff}}^{\uparrow\downarrow}]$) equals 1.81, which is in agreement with the orders of magnitude for ratios that can be inferred from the results of Mizukami *et al.* [22] (≈ 5) or Nan *et al.* [32] (≈ 3.8) for Permalloy/Pt bilayers. On the other hand, a relatively high value of $\text{Im}[g_{\text{eff}}^{\uparrow\downarrow}]$ for Finemet/Ta bilayers leads to $\delta\alpha/\delta g/g_0 = 0.38$. According to the microscopic theory, the difference between those two ratios originates from disparate values of the hopping amplitudes or spin-orbit interaction [see Eq. (8)].

B. Interfacial heavy-metal-induced anisotropy

In thin magnetic films a standard way to account for surface-induced effects is through surface anisotropy, i.e., $4\pi M_{\text{eff}} = 4\pi M_s - H_{\perp}$, where H_{\perp} is the surface anisotropy field that is usually perpendicular to the surface. In NM/FM bilayers, within an emergence of the interfacial spin-orbit coupling, we may expect variations in the effective magnetization caused by an additional surface anisotropy field due to NM coverage of a FM film. As shown in Figs. 6(a) and 6(b), the value of $4\pi M_{\text{eff}}$ for a bare Finemet film considerably increases with the appearance of both Pt and Ta layers. To quantitatively evaluate the magnitude of this effect, we can directly distinguish the surface anisotropy field H_{HM} (induced solely by a heavy metal) and write

$$4\pi M_{\text{eff}} = (4\pi M_s - H_{\perp}) - H_{\text{HM}}, \quad (12)$$

with

$$H_{\text{HM}} = \frac{2K_{\text{HM}}}{M_s d_F}. \quad (13)$$

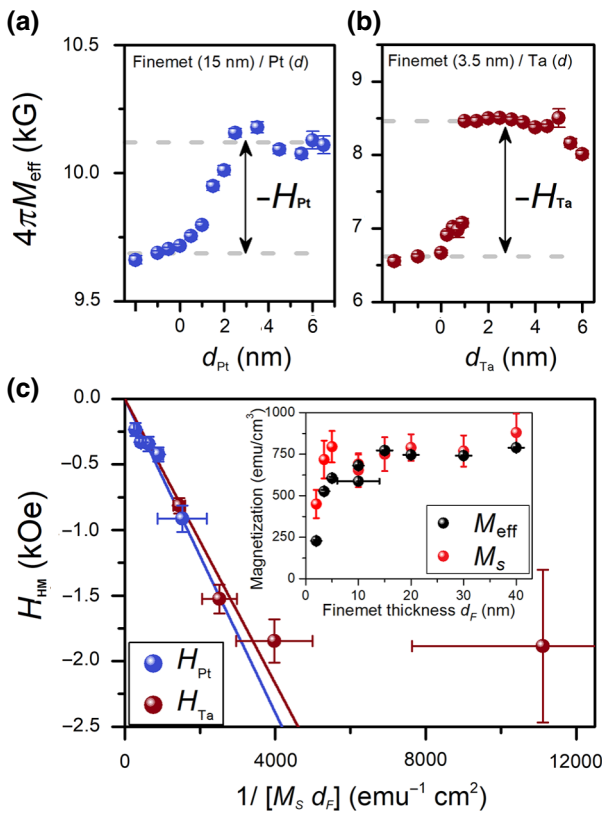


FIG. 6. Effective magnetization versus thickness for (a) Pt and (b) Ta layers for a fixed thickness of Finemet film. The values of $4\pi M_{\text{eff}}$ below zero thickness for the heavy-metal film derive from separate measurements of the lone Finemet film taken at different positions outside the heavy-metal wedge. In (c) changes in the anisotropy field $H_{\text{Pt,Ta}}$ caused by the appearance of the heavy-metal film are plotted as a function of $M_s^{-1}d_F^{-1}$. The solid lines represent the fit according to Eq. (13). The inset shows values of the effective magnetization and the saturation magnetization of lone Finemet films of different thicknesses.

To determine the anisotropy constant $K_{\text{HM}=\text{Pt,Ta}}$, we plot the $H_{\text{HM}}(M_s^{-1}d_F^{-1})$ dependence in Fig. 6(c). The value of $-H_{\text{HM}}$ increases as the thickness of the Finemet decreases, what indicates the interfacial origin of this anisotropy field. For Finemet films covered with Pt, the value of $2K_{\text{Pt}}$ equals -0.60 ± 0.06 erg/cm², while for samples with Ta, $2K_{\text{Pt}} = -0.54 \pm 0.04$ erg/cm², as fitted with Eq. (13). In our convention, a negative K_{HM} signifies the in-plane anisotropy contribution counterbalancing H_{\perp} . For Finemet(2 nm)/Ta bilayers, we note that H_{Ta} significantly deviates from the relation given by Eq. (13), yielding $2K_{\text{Ta}} = -0.17 \pm 0.07$ erg/cm². The value, however, is determined with a large standard error arising from the uncertainty of measuring M_s , d_F , and H_{Ta} due to variations in M_{eff} . Nevertheless, the appearance of an anisotropy field induced by the heavy metals and systematic changes to H_{HM} as a function of thickness may provide the initial indication of spin-orbit

coupling occurring at the heavy-metal–ferromagnet interface.

C. Interface spin-orbit interaction and hopping amplitudes

By combining Eqs. (6) and (7) (see the derivation in the Supplemental Material [42]) we obtain the following simple quadratic equation with respect to the hopping amplitudes \tilde{t}_σ^0 :

$$\frac{m_e^2 a^5}{2\pi^2 d_F \hbar^4} (\tilde{t}_\sigma^0)^2 - \frac{\delta g/g_0}{\tilde{\gamma}_{xz}} \tilde{t}_\sigma^0 + \delta \alpha = 0. \quad (14)$$

This is equivalent to

$$\frac{m_e^2 a^5}{2\pi^2 \hbar^4} \frac{4\pi M_S}{g_0 \mu_B} (\tilde{t}_\sigma^0)^2 - \frac{\text{Im}[g_{\text{eff}}^{\uparrow\downarrow}]}{\tilde{\gamma}_{xz}} \tilde{t}_\sigma^0 + \text{Re}[g_{\text{eff}}^{\uparrow\downarrow}] = 0, \quad (15)$$

where $\sigma = \uparrow, \downarrow$.

The real roots are obtained for $\tilde{\gamma}_{xz} \leq \tilde{\gamma}_{xz}^{\max}$, where $\tilde{\gamma}_{xz}^{\max} = \sqrt{(\pi \hbar^4 g_0 \mu_B / 8m_e^2 a^5 M_S)(\text{Im}[g_{\text{eff}}^{\uparrow\downarrow}]^2 / \text{Re}[g_{\text{eff}}^{\uparrow\downarrow}])}$. It is important to emphasize at this point that $\text{Im}[g_{\text{eff}}^{\uparrow\downarrow}] \neq 0$ gives rise to a finite value of the interface spin-orbit parameter $\tilde{\gamma}_{xz}$. In particular, for $\tilde{\gamma}_{xz} = \tilde{\gamma}_{xz}^{\max}$, the hopping amplitudes have equal values, $\tilde{t}_\uparrow^0 = \tilde{t}_\downarrow^0 = \sqrt{(\pi \hbar^4 g_0 \mu_B / 2m_e^2 a^5 M_S) \text{Re}[g_{\text{eff}}^{\uparrow\downarrow}]}$.

For the experimentally derived parameters of the studied bilayers, the possible solutions of Eq. (15) are plotted in Fig. 7. Solutions of Eq. (15) represent the asymmetrical bell-like curves: flat for high ratios of $\text{Re}[g_{\text{eff}}^{\uparrow\downarrow}] / \text{Im}[g_{\text{eff}}^{\uparrow\downarrow}]$ and slender otherwise. For comparison, a flat curve typical of Permalloy/Pt bilayers is also plotted according to parameters found in Ref. [22], resulting in a $\text{Re}[g_{\text{eff}}^{\uparrow\downarrow}] / \text{Im}[g_{\text{eff}}^{\uparrow\downarrow}]$ ratio of 5. It is hard to unambiguously pinpoint possible values for the hopping amplitudes $\tilde{t}_{\uparrow,\downarrow}^0$ and spin-orbit interaction $\tilde{\gamma}_{xz}$. Nevertheless, it is possible to qualitatively determine the reasonable energy ranges for which these parameters have a physical sense. We assume that the $\tilde{t}_{\uparrow,\downarrow}^0$ values are in the range 0–1.5 eV and that the $\tilde{\gamma}_{xz}$ values are of the order of several hundred meV. The former condition is fulfilled in the shaded areas of Fig. 7 next to $\tilde{\gamma}_{xz}^{\max}$, i.e., for very different values of $\tilde{\gamma}_{xz}$ for Pt (approximately 300 meV) and Ta (approximately 600 meV). On the other hand, for similar and reasonable $\tilde{\gamma}_{xz}$ values of about 250–350 meV for both Ta and Pt the $\tilde{\gamma}_{xz}(\tilde{t}_\uparrow^0 + \tilde{t}_\downarrow^0)$ are almost equal (according to the experiment), but the asymmetry of the $\tilde{t}_{\uparrow,\downarrow}^0$ values is significant, about 2 eV. Which of the scenarios is closer to reality is an open question—the more so given that the parameters appearing in Eq. (15) result from several simplifications.

An alternative approach to the spin-pumping quantum mechanical formalism with hopping amplitudes \tilde{t}_\uparrow^0 and \tilde{t}_\downarrow^0 is

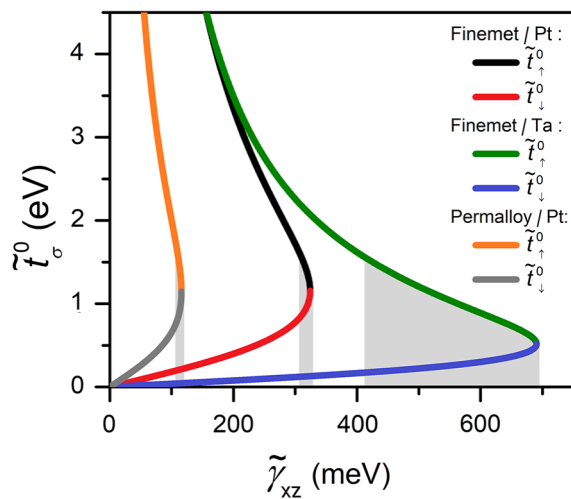


FIG. 7. Hopping amplitudes \tilde{t}_σ^0 versus interface spin-orbit interactions $\tilde{\gamma}_{xz}$ for Finemet/Pt and Finemet/Ta bilayers. For comparison, the curves for the Permalloy/Pt bilayer are plotted according to parameters found in Ref. [22]. The lattice constant is taken from Ref. [64] (3.5 Å).

based on the spin-exchange interaction between localized moments and conductivity electrons [16]. This simplistic model offers a comprehensive insight into complex phenomena related to spin pumping. The key parameters underlying the deterministic material properties in this model are the electrical resistivity ρ_N and the spin-diffusion length λ_N of nonmagnetic material [see Eq. (60) of Ref. [16]]:

$$\text{Re}[g_{\uparrow\downarrow}] \approx \frac{h}{e^2} \frac{1}{\rho_N \lambda_N}. \quad (16)$$

Here $h/e^2 \approx 25.8 \text{ k}\Omega.$ is the quantum of resistance. Equation (16) is valid for a transparent interface, that is, for no spin-orbit coupling, and represents the lowest limit of $G_{\uparrow\downarrow}$ (or $g_{\uparrow\downarrow} = (h/e^2)G_{\uparrow\downarrow}$) [16].

For typical parameters ($\lambda_{\text{Pt}} = 10 \text{ nm}$, $\rho_{\text{Pt}} = 10 \mu\Omega \text{ cm}$) [65], $\text{Re}[g_{\uparrow\downarrow}] \approx 2.6 \times 10^{15} \text{ cm}^{-2}$, while for Ta with a substantially lower value of $\lambda_{\text{Ta}} = 2 \text{ nm}$ and a higher resistivity of $340 \mu\Omega \text{ cm}$ [65], $\text{Re}[g_{\uparrow\downarrow}] \approx 0.4 \times 10^{15} \text{ cm}^{-2}$. Our estimation roughly agrees with the experimental data, but the agreement may be accidental. Nevertheless, Eq. (16) gives a realistic qualitative insight into the impact of material parameters on $\text{Re}[G_{\uparrow\downarrow}]$. A high resistivity, together with a comparably low spin-diffusion length, results in a small $\text{Re}[G_{\uparrow\downarrow}]$ when Ta is chosen as a capping layer. Moreover, within the approach of Takahashi [16], we can also estimate the ratio

$$\frac{\text{Re}[G_{\uparrow\downarrow}]}{\text{Im}[G_{\uparrow\downarrow}]} \approx \frac{\tau_{\text{ex}} \lambda_N}{\tau_N a}, \quad (17)$$

where $\tau_{\text{ex}} = \hbar/SJ_{sd}$ is the exchange relaxation time, τ_N is the spin-flip relaxation time, a is the lattice constant, S is the spin value, J_{sd} is the exchange interaction constant and \hbar is the reduced Planck constant. If we roughly approximate τ_{ex} by τ_{tr} —the electron transport relaxation time [see Eq. (12.30) of Ref. [65]]—we arrive at the ratio $\sqrt{\tau_{\text{tr}}/\tau_N} \approx \xi/\rho_N \lambda_N$, where $\xi = (\sqrt{3\pi}/2k_F^2)\hbar/e^2 \approx 7 \times 10^{-12} \Omega \text{ cm}^2$ and k_F is the Fermi wave vector of $1 \times 10^8 \text{ cm}^{-1}$. Hence,

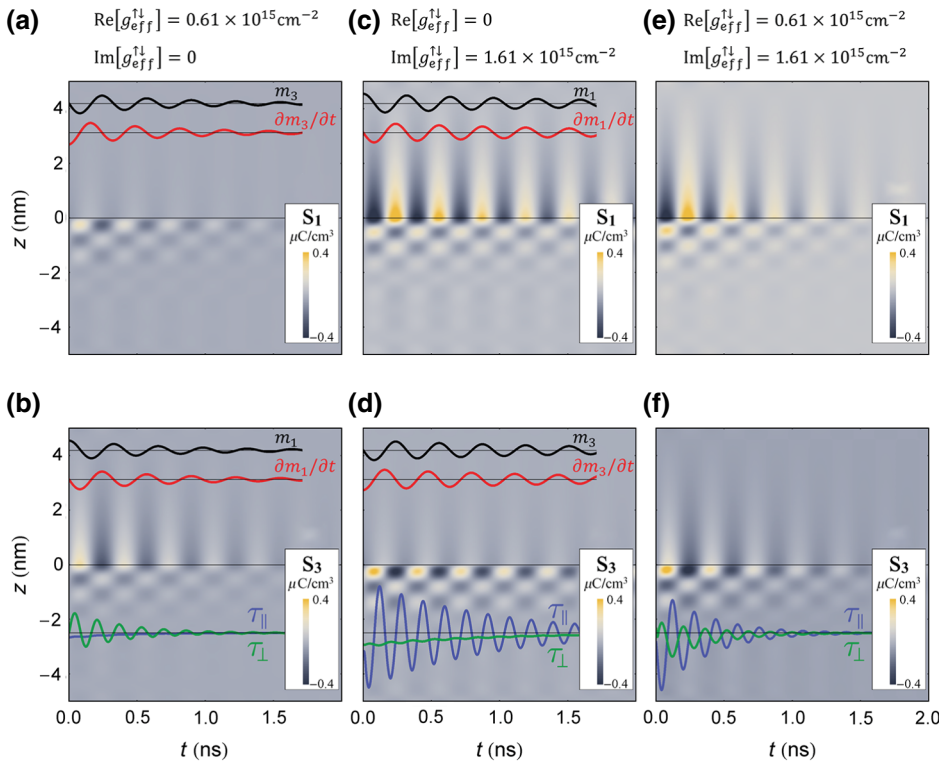
$$\frac{\text{Re}[G_{\uparrow\downarrow}]}{\text{Im}[G_{\uparrow\downarrow}]} \approx \frac{4\xi^2}{a\rho_N^2 \lambda_N} = \frac{1/(\rho_N \lambda_N)}{1/(2\xi/a)(2\xi/\rho_N)} = \frac{1/(\rho_N \lambda_N)}{1/(\rho^* \lambda^*)}. \quad (18)$$

The nominator $1/(\rho_N \lambda_N)$ has the meaning of $\text{Re}[G_{\uparrow\downarrow}]$ in $\Omega^{-1} \text{ cm}^{-2}$. The meaning of the denominator $1/(2\xi/a)(2\xi/\rho_N)$ is less clear, but if we decompose it to mirror the form of the nominator, its meaning is straightforward. The value $\rho^* = 468 \mu\Omega \text{ cm}$ is determined by the electronic structure of the interface and may be regarded as the interface resistivity. The value of λ^* determines in some way the spin-diffusion length across an interface. For the assumed ρ_N values, λ^* is 14 nm for Pt and only 0.4 nm for Ta, so that $\text{Re}[G_{\uparrow\downarrow}]/\text{Im}[G_{\uparrow\downarrow}] \approx 65$ and 0.3 for F/Pt and F/Ta bilayers, respectively.

The estimated λ^* value of 14 nm for F/Pt bilayers is much too high since a ratio of approximately 65 is much higher than that found experimentally (approximately 2). Our estimation of $\text{Re}[G_{\uparrow\downarrow}]/\text{Im}[G_{\uparrow\downarrow}]$ in the framework of the model of Takahashi [16] does not assume any spin-orbit coupling so, for a generally accepted set of ρ_N and λ_N values [65], the ratio attains values not found in our experiment (for F/Pt mainly). Therefore, by taking λ^* as a free parameter resulting from interfacial spin-orbit coupling, we can roughly estimate its impact on the ratio $\text{Re}[G_{\uparrow\downarrow}]/\text{Im}[G_{\uparrow\downarrow}]$. If we take λ^* to be 0.4 nm, $\text{Re}[G_{\uparrow\downarrow}]/\text{Im}[G_{\uparrow\downarrow}]$ is 2, in agreement with the experiment for F/Pt bilayers.

D. Impact of the imaginary part of the spin-mixing conductance on magnetization dynamics

Since Finemet/Ta bilayers exhibit distinctively different properties from Finemet/Pt bilayers, namely the imaginary part of the spin-mixing conductance of the former is higher than the real part, using the diffusive model, we investigate the spin-magnetization dynamics in this particular system. The coupled differential equations for the magnetization \vec{m} , spin accumulation \vec{s} , and spin current \vec{J}_s , with spin pumping at the Finemet/Ta interface and spin torque (ST) terms, are solved numerically in the time-dependent COMSOL Multiphysics model (see the Supplemental Material [42] for detailed information). The magnetization deviates from the equilibrium direction along the \hat{x}_2 axis to $\vec{m}_0 = (10 \text{ A/m}, M_s, 0)$ at $t = 0$, and its precession is subject to the Gilbert damping and STs.



Due to the spin pumping, an additional spin flux [see Eq. (S15) in the Supplemental Material [42]] results in the flow of the nonequilibrium spin density \vec{s} away from the Finemet/Ta interface. In Finemet, the spin accumulation interacts with the magnetization through the ST. In the case of a thin Ta film, i.e., if $d_{\text{Ta}} \ll \lambda_{\text{SF}}$, the spin-pumping flow is immediately balanced by the spin accumulation gradient at the opposite Ta surface and the overall influence on the magnetization dynamics is reduced. Otherwise, for a thick Ta film (as used in the experimentally investigated samples), the spin relaxation in Ta leads to the loss of total angular momentum in the system and, consequently, the damping and the frequency shift of the magnetization dynamics are enhanced in Finemet.

We show in Fig. 8 a temporal evolution of spin accumulation \vec{s} through a thickness of Ta and Finemet (yellow and grey maps). The real part of the spin-mixing conductance $\text{Re}[g_{\text{eff}}^{\uparrow\downarrow}]$ produces a spin current and a spin accumulation at the F/Ta interface: $(s_1, 0, s_3) \propto (\delta m_3 / \delta t, 0, \delta m_1 / \delta t)$; see Figs. 8(a) and 8(b). The imaginary part of the spin-mixing conductance $\text{Im}[g_{\text{eff}}^{\uparrow\downarrow}]$ on the other hand produces a spin current and a spin accumulation at the F/Ta interface: $(s_1, 0, s_3) \propto (\delta m_1 / \delta t, 0, \delta m_3 / \delta t)$; see Figs. 8(c) and 8(d). The difference in amplitudes between s_1 and s_3 results from the ellipticity of magnetization precession and the higher value of the in-plane component m_1 in relation to m_3 . It is clear that, for the system with Ta, the spin accumulation is governed by $\text{Im}[g_{\text{eff}}^{\uparrow\downarrow}]$, which arises from the ratio $\text{Re}[g_{\text{eff}}^{\uparrow\downarrow}] / \text{Im}[g_{\text{eff}}^{\uparrow\downarrow}] = 0.38$. Figures 8(e) and

FIG. 8. The coupled spin-magnetization dynamics in the Finemet/Ta bilayer. Temporal and spatial distributions of the components \vec{s} (s_1 , upper panel, and s_3 , bottom panel; yellow and grey maps) compared with the temporal evolution of \vec{m} (black lines) and its derivative (red lines) as a consequence of the spin pumping driven by the real part [(a),(b)], the imaginary part [(c),(d)], and the total [(e),(f)] spin-mixing conductance. The amplitudes of \vec{m} components are normalized for clarity. The blue and green lines in (b), (d), and (f) show the values of the spin-transfer torque parallel and perpendicular to the dynamic components of magnetization. In the adopted reference system $z = 0$ nm corresponds to the Finemet/Ta interface. The area below ($z < 0$) shows the Finemet film and the area above ($z > 0$) shows the Ta film.

8(f) show the overall dynamics of \vec{s} due to both $\text{Im}[g_{\text{eff}}^{\uparrow\downarrow}]$ and $\text{Re}[g_{\text{eff}}^{\uparrow\downarrow}]$, which can also be viewed as a resultant of the amplitudes shown in (a), (c) and (b), (d), respectively.

At a given time, spin accumulation decays exponentially in Ta by a factor of $1/e$ at a distance λ_{SF} from the interface. In Finemet, \vec{s} rotates around \vec{m} along the direction $-\hat{x}_3$ from the F/Ta interface (with the characteristic length $2\pi\lambda_L = 1.8$ nm), leading to the oscillatory behavior of \vec{s} components across Finemet thicknesses. Since we assume a linear regime of magnetization dynamics, $\vec{m} \approx M_s \hat{x}_2$, then \vec{s} is always perpendicular to \vec{m} and decays with the characteristic length $\lambda_\perp = 1.2$ nm.

To elucidate the influence of $\text{Re}[g_{\text{eff}}^{\uparrow\downarrow}]$ and $\text{Im}[g_{\text{eff}}^{\uparrow\downarrow}]$ on the temporal evolution of the magnetization, we calculate the spin torque in Finemet that is parallel to the dynamic magnetization ($\vec{\tau}_{\parallel}$), and, thus, it is responsible for the damping and ST perpendicular to the dynamic magnetization ($\vec{\tau}_\perp$), responsible for a change of the frequency of the precession (see the Supplemental Material [42]). The values of the STs have been integrated over the thickness of Finemet and plotted in Fig. 8. The magnitude of the perpendicular component of the ST, τ_\perp , generated by the real part of the spin-mixing conductance [green line in Fig. 8(b)], oscillates with double the FMR frequency. Therefore, the time-averaged value of τ_\perp is zero and the frequency of precession of \vec{m} is not affected. On the other hand, the value of the parallel component of the ST, τ_{\parallel} [blue line in Fig. 8(b)], has a negative sign at any time. This means that the ST is always antiparallel to the dynamic components

of magnetization, leading to the enhanced damping. For the imaginary part of the spin-mixing conductance, it is τ_{\parallel} that oscillates with a frequency that is double the FMR frequency [blue line in Fig. 8(d)], resulting in almost zero damping. The value of the perpendicular component of the ST, τ_{\perp} [green line in Fig. 8(d)], has a negative sign at any time, acting always to increase the frequency of precession. In Fig. 8(f) the overall STs are shown, which are the sum of the influence of the real and imaginary parts of the spin-mixing conductance.

VI. CONCLUSIONS

In summary, we show that the investigated spin-pumping effect in Finemet films with Pt and Ta capping layers results in linear dependencies of the Gilbert damping parameter and the g-factor shift on the inverse Finemet thickness, which subsequently allows us to determine both the real and imaginary parts of the spin-mixing conductance. We find that replacing Pt with Ta as a capping layer results in a fivefold decrease of $\text{Re}[g_{\text{eff}}^{\uparrow\downarrow}]$. On the other hand, $\text{Im}[g_{\text{eff}}^{\uparrow\downarrow}]$ is nearly the same for Pt and Ta capping layers. Therefore, the magnetization dynamics in Finemet/Ta bilayers is apparently governed by the dominant role of $\text{Im}[g_{\text{eff}}^{\uparrow\downarrow}]$. Giving insight into the microscopic origin of spin pumping, we conclude that the main difference between spin pumping in F/Pt and F/Ta bilayers can be understood in terms of the interplay between hopping amplitudes $t_{\uparrow\downarrow}^0$ and the strength of the interfacial spin-orbit coupling γ_{xz} [cf. Eq. (15) and Fig. 7]. We also qualitatively discuss the experimental results in terms of a simplistic model. It appears that the real part of the spin-mixing conductance is proportional to $1/(\rho_N \lambda_N)$, where ρ_N is the resistivity and λ_N is the spin-diffusion length of a nonmagnetic metal. It confirms, in accordance with Ref. [20], that $\text{Re}[g_{\text{eff}}^{\uparrow\downarrow}]$ of metallic FM/NM interfaces is mainly determined by the NM layers. By contrast, the imaginary part of the spin-mixing conductance is proportional to $1/(\rho^* \lambda^*)$, where ρ^* is determined by an electronic structure of an interface while λ^* is related in some way to the spin diffusion across an interface. This may clarify the role of material and interface transport parameters that give rise to the estimated magnitudes of the complex spin-mixing conductance (i.e., the real and imaginary parts of the spin-mixing conductance).

ACKNOWLEDGMENTS

This work was supported by the project “Marie Skłodowska-Curie Research and Innovation Staff Exchange (RISE)” Contract No. 644348 with the European Commission, as part of the Horizon2020 Programme. A.K. acknowledges the support from program POWR.03.02.00-00-I032/16.

- [1] DongJoon Lee, JongHyuk Kim, HeeGyun Park, Kyung-Jin Lee, Byeong-Kwon Ju Hyun Cheol Koo, Byoung-Chul Min, and OukJae Lee, Spin-Orbit Torque and Magnetic Damping in Tailored Ferromagnetic Bilayers, *Phys. Rev. Appl.* **10**, 024029 (2018).
- [2] G. Prenat, K. Jabeur, P. Vanhauwaert, G. D. Pendina, F. Oboril, R. Bishnoi, M. Ebrahimi, N. Lamard, O. Boulle, K. Garello, J. Langer, B. Ocker, M. Cyrille, P. Gambardella, M. Tahoori, and G. Gaudin, Ultra-fast and high-reliability SOT-MRAM: From cache replacement to normally-off computing, *IEEE Trans. Multi-Scale Comput. Syst.* **2**, 49 (2016).
- [3] Mukund Bapna, Brad Parks, Samuel D. Oberdick, Hamid Almasi, Weigang Wang, and Sara A. Majetich, Spin-Orbit-Torque Switching in 20-nm Perpendicular Magnetic Tunnel Junctions, *Phys. Rev. Appl.* **10**, 024013 (2018).
- [4] Weijia Fan, Jie Zhao, Meng Tang, Huanjian Chen, Huanglin Yang, Weiming Lü, Zhong Shi, and Xuepeng Qiu, Asymmetric Spin-Orbit-Torque-Induced Magnetization Switching with a Noncollinear In-Plane Assisting Magnetic Field, *Phys. Rev. Appl.* **11**, 034018 (2019).
- [5] R. Bishnoi, F. Oboril, and M. B. Tahoori, in *2016 International Great Lakes Symposium on VLSI (GLSVLSI)* (Association for Computing Machinery, New York, NY, United States, 2016), p. 409.
- [6] V. Sverdlov, A. Makarov, and S. Selberherr, in *2018 Joint International EUROSOI Workshop and International Conference on Ultimate Integration on Silicon (EUROSOI-ULIS)* (IEEE, Granada, Spain, 2018), p. 1.
- [7] Qianchang Wang, John Domann, Guoqiang Yu, Anthony Barra, Kang L. Wang, and Gregory P. Carman, Strain-Mediated Spin-Orbit-Torque Switching for Magnetic Memory, *Phys. Rev. Appl.* **10**, 034052 (2018).
- [8] Arnab Bose, Hanuman Singh, Varun Kumar Kushwaha, Swapnil Bhuktare, Sutapa Dutta, and Ashwin A. Tulpapurkar, Sign Reversal of Fieldlike Spin-Orbit Torque in an Ultrathin Cr/Ni Bilayer, *Phys. Rev. Appl.* **9**, 014022 (2018).
- [9] Q. Y. Wong, C. Murapaka, W. C. Law, W. L. Gan, G. J. Lim, and W. S. Lew, Enhanced Spin-Orbit Torques in Rare-Earth Pt/Co/Ni₂/Co/Tb Systems, *Phys. Rev. Appl.* **11**, 024057 (2019).
- [10] Hyung Keun Gweon, Kyung-Jin Lee, and Sang Ho Lim, Influence of MgO Sputtering Power and Post Annealing on Strength and Angular Dependence of Spin-Orbit Torques in Pt/Co/MgO Trilayers, *Phys. Rev. Appl.* **11**, 014034 (2019).
- [11] Kevin Garello, Ioan Mihai Miron, Can Onur Avci, Frank Freimuth, Yuriy Mokrousov, Stefan Blügel, Stéphane Aufret, Olivier Boulle, Gilles Gaudin, and Pietro Gambardella, Symmetry and magnitude of spin-orbit torques in ferromagnetic heterostructures, *Nat. Nanotechnol.* **8**, 587 (2013).
- [12] Lijun Zhu, Daniel. C. Ralph, and Robert A. Buhrman, Highly Efficient Spin-Current Generation by the Spin Hall Effect in Au_{1-x}Pt_x, *Phys. Rev. Appl.* **10**, 031001 (2018).
- [13] Rajagopalan Ramaswamy, Yi Wang, Mehrdad Elyasi, M. Motapothula, T. Venkatesan, Xuepeng Qiu, and Hyunsoo Yang, Extrinsic Spin Hall Effect in Cu_{1-x}Pt_x, *Phys. Rev. Appl.* **8**, 024034 (2017).

- [14] Weifeng Zhang, Wei Han, Xin Jiang, See-Hun Yang, and Stuart S. P. Parkin, Role of transparency of platinum-ferromagnet interfaces in determining the intrinsic magnitude of the spin Hall effect, *Nat. Phys.* **11**, 496 (2015).
- [15] Kyoung-Whan Kim, Kyung-Jin Lee, Jairo Sinova, Hyun-Woo Lee, and M. D. Stiles, Spin-orbit torques from interfacial spin-orbit coupling for various interfaces, *Phys. Rev. B* **96**, 104438 (2017).
- [16] Saburo Takahashi, in *Handbook of Spintronics*, edited by Yongbing Xu, David D. Awschalom, and Junsaku Nitta (Springer, Netherlands, Dordrecht, 2016), p. 1445.
- [17] K. Sato, E. Saitoh, A. Willoughby, P. Capper, and S. Kasap, *Spintronics for Next Generation Innovative Devices* (John Wiley and Sons, Hoboken, NJ, 2015).
- [18] S Azzawi, A. T. Hindmarch, and D Atkinson, Magnetic damping phenomena in ferromagnetic thin-films and multilayers, *J. Phys. D: Appl. Phys.* **50**, 473001 (2017).
- [19] Yi Wang, Rajagopal Ramaswamy, and Hyunsoo Yang, FMR-related phenomena in spintronic devices, *J. Phys. D: Appl. Phys.* **51**, 273002 (2018).
- [20] F. D. Czeschka, L. Dreher, M. S. Brandt, M. Weiler, M. Althammer, I.-M. Imort, G. Reiss, A. Thomas, W. Schoch, W. Limmer, H. Huebl, R. Gross, and S. T. B. Goennenwein, Scaling Behavior of the Spin Pumping Effect in Ferromagnet-Platinum Bilayers, *Phys. Rev. Lett.* **107**, 046601 (2011).
- [21] H. Główski, F. Lisiecki, P. Kuświk, J. Dubowik, and F. Stobiecki, Influence of adjacent layers on the damping of magnetization precession in $\text{Co}_x\text{Fe}_{100-x}$ films, *J. Alloys Compd.* **785**, 891 (2019).
- [22] Shigemi Mizukami, Yasuo Ando, and Terunobu Miyazaki, The study on ferromagnetic resonance linewidth for NM/80NiFe/NM (NM = Cu, Ta, Pd and Pt) films, *Jpn. J. Appl. Phys.* **40**, 580 (2001).
- [23] Justin M. Shaw, Erna K. Delczeg-Czirjak, Eric R. J. Edwards, Yaroslav Kvashnin, Danny Thonig, Martin A. W. Schoen, Matt Pufall, Michael L. Schneider, Thomas J. Silva, Olof Karis, Katherine P. Rice, Olle Eriksson, and Hans T. Nembach, Magnetic damping in sputter-deposited Co_2MnGe Heusler compounds with $A2$, $B2$, and $L2_1$ orders: Experiment and theory, *Phys. Rev. B* **97**, 094420 (2018).
- [24] Gary Allen, Sasikanth Manipatruni, Dmitri E. Nikonorov, Mark Doczy, and Ian A. Young, Experimental demonstration of the coexistence of spin Hall and Rashba effects in β -tantalum/ferromagnet bilayers, *Phys. Rev. B* **91**, 144412 (2015).
- [25] Eric Montoya, Pavlo Omelchenko, Chris Coutts, Nicholas R. Lee-Hone, René Hübler, David Broun, Bret Heinrich, and Erol Girt, Spin transport in tantalum studied using magnetic single and double layers, *Phys. Rev. B* **94**, 054416 (2016).
- [26] Ledong Wang, Zhijian Lu, Jianshu Xue, Peng Shi, Yufeng Tian, Yanxue Chen, Shishen Yan, Lihui Bai, and Michael Harder, Electrical Control of Spin-Mixing Conductance in a $\text{Y}_3\text{Fe}_5\text{O}_{12}$ /Platinum Bilayer, *Phys. Rev. Appl.* **11**, 044060 (2019).
- [27] Jungbum Yoon, Seo-Won Lee, Jae Hyun Kwon, Jong Min Lee, Jaesung Son, Xuepeng Qiu, Kyung-Jin Lee, and Hyunsoo Yang, Anomalous spin-orbit torque switching due to field-like torque-assisted domain wall reflection, *Sci. Adv.* **3**, e1603099 (2017).
- [28] James Lourembam, Abhijit Ghosh, Minggang Zeng, Seng Kai Ong, Qi Jia Yap, and Sze Ter Lim, Thickness-Dependent Perpendicular Magnetic Anisotropy and Gilbert Damping in $\text{Hf}/\text{Co}_{20}\text{Fe}_{60}\text{B}_{20}/\text{MgO}$ Heterostructures, *Phys. Rev. Appl.* **10**, 044057 (2018).
- [29] K. Xia, P. J. Kelly, G. E. W. Bauer, A. Brataas, and I. Turek, Spin torques in ferromagnetic/normal-metal structures, *Phys. Rev. B* **65**, 220401 (2002).
- [30] Paul M. Haney, Hyun-Woo Lee, Kyung-Jin Lee, Aurélien Manchon, and M. D. Stiles, Current induced torques and interfacial spin-orbit coupling: Semiclassical modeling, *Phys. Rev. B* **87**, 174411 (2013).
- [31] V. P. Amin and M. D. Stiles, Spin transport at interfaces with spin-orbit coupling: Phenomenology, *Phys. Rev. B* **94**, 104420 (2016).
- [32] Tianxiang Nan, Satoru Emori, Carl T. Boone, Xinjun Wang, Trevor M. Oxholm, John G. Jones, Brandon M. Howe, Gail J. Brown, and Nian X. Sun, Comparison of spin-orbit torques and spin pumping across NiFe/Pt and NiFe/Cu/Pt interfaces, *Phys. Rev. B* **91**, 214416 (2015).
- [33] Yiyuan Sun, Houchen Chang, Michael Kabatek, Young-Yeal Song, Zihui Wang, Michael Jantz, William Schneider, Mingzhong Wu, E. Montoya, B. Kardasz, B. Heinrich, Suzanne G. E. te Velthuis, Helmut Schultheiss, and Axel Hoffmann, Damping in Yttrium Iron Garnet Nanoscale Films Capped by Platinum, *Phys. Rev. Lett.* **111**, 106601 (2013).
- [34] Adam B. Cahaya, Alejandro O. Leon, and Gerrit E. W. Bauer, Crystal field effects on spin pumping, *Phys. Rev. B* **96**, 144434 (2017).
- [35] H. Nakayama, M. Althammer, Y.-T. Chen, K. Uchida, Y. Kajiwara, D. Kikuchi, T. Ohtani, S. Geprägs, M. Opel, S. Takahashi, R. Gross, G. E. W. Bauer, S. T. B. Goennenwein, and E. Saitoh, Spin Hall Magnetoresistance Induced by a Nonequilibrium Proximity Effect, *Phys. Rev. Lett.* **110**, 206601 (2013).
- [36] Tobias Kosub, Saül Vélez, Juan M. Gomez-Perez, Luis E. Hueso, Jürgen Fassbender, Felix Casanova, and Denys Makarov, Anomalous Hall-like transverse magnetoresistance in Au thin films on $\text{Y}_3\text{Fe}_5\text{O}_{12}$, *Appl. Phys. Lett.* **113**, 222409 (2018).
- [37] N. Vlietstra, J. Shan, V. Castel, J. Ben Youssef, G. E. W. Bauer, and B. J. van Wees, Exchange magnetic field torques in YIG/Pt bilayers observed by the spin-Hall magnetoresistance, *Appl. Phys. Lett.* **103**, 032401 (2013).
- [38] M. Cecot, Ł. Karwacki, W. Skowroński, J. Kanak, J. Wrona, A. Żywczałk, L. Yao, S. van Dijken, J. Barnaś, and T. Stobiecki, Influence of intermixing at the Ta/CoFeB interface on spin Hall angle in Ta/CoFeB/MgO heterostructures, *Sci. Rep.* **7**, 968 (2017).
- [39] Gen Tatara and Shigemi Mizukami, Consistent microscopic analysis of spin pumping effects, *Phys. Rev. B* **96**, 064423 (2017).
- [40] Yaroslav Tserkovnyak, Arne Brataas, Gerrit E. W. Bauer, and Bertrand I. Halperin, Nonlocal magnetization dynamics

- in ferromagnetic heterostructures, *Rev. Mod. Phys.* **77**, 1375 (2005).
- [41] M. Zwierzycki, Y. Tserkovnyak, P. J. Kelly, A. Brataas, and G. E. W. Bauer, First-principles study of magnetization relaxation enhancement and spin transfer in thin magnetic films, *Phys. Rev. B* **71**, 064420 (2005).
- [42] See Supplemental Material at <http://link.aps.org/supplemental/10.1103/PhysRevApplied.13.054011> for residual analysis, derivation of the equation for hopping amplitudes and spin-orbit interaction, the model of magnetization dynamics, magnetic measurements, and VNA-FMR data.
- [43] H. Głowiński, I. Gościańska, A. Krysztofik, J. Barnaś, M. Cecot, P. Kuświk, and J. Dubowik, in *2016 21st International Conference on Microwave, Radar and Wireless Communications (MIKON)* (IEEE, Krakow, Poland, 2016), p. 1.
- [44] E. Coy, I. Fina, K. Załęski, A. Krysztofik, L. Yate, L. Rodriguez, P. Graczyk, H. Głowiński, C. Ferrater, J. Dubowik, and M. Varela, High-Temperature Magnetodielectric $\text{Bi}(\text{Fe}_{0.5}\text{Mn}_{0.5})\text{O}_3$ Thin Films with Checkerboard-Ordered Oxygen Vacancies and Low Magnetic Damping, Supplementary Materials, *Phys. Rev. Appl.* **10**, 054072 (2018).
- [45] I. Gościańska, J. Dubowik, H. Ratajczak, M. Konč, and P. Sovák, Magnetic properties of Al-substituted finemet-type $\text{Fe}_{73.5-x}\text{Al}_x\text{Cu}_1\text{Nb}_3\text{Si}_{13.5}\text{B}_9$ thin films, *J. Magn. Magn. Mater.* **242–245**, 177 (2002).
- [46] M. J. P. Alves, D. E. Gonzalez-Chavez, F. Bohn, and R. L. Sommer, Annealing effects on the microwave linewidth broadening of FeCuNbSiB ferromagnetic films, *J. Appl. Phys.* **117**, 123913 (2015).
- [47] D. R. G. Mitchell, DiffTools: Electron diffraction software tools for DigitalMicrographTM, *Microsc. Res. Tech.* **71**, 588 (2008).
- [48] H. Głowiński, M. Schmidt, I. Gościańska, J.-Ph. Ansermet, and J. Dubowik, Coplanar waveguide based ferromagnetic resonance in ultrathin film magnetic nanostructures: Impact of conducting layers, *J. Appl. Phys.* **116**, 053901 (2014).
- [49] P. Kuświk, H. Głowiński, E. Coy, J. Dubowik, and F. Stobiecki, Perpendicularly magnetized $\text{Co}_{20}\text{Fe}_{60}\text{B}_{20}$ layer sandwiched between Au with low Gilbert damping, *J. Phys.: Condens. Matter* **29**, 435803 (2017).
- [50] C. T. Boone, J. M. Shaw, H. T. Nembach, and T. J. Silva, Spin-scattering rates in metallic thin films measured by ferromagnetic resonance damping enhanced by spin-pumping, *J. Appl. Phys.* **117**, 223910 (2015).
- [51] A. Conca, S. Keller, L. Mihalceanu, T. Kehagias, G. P. Dimitrakopoulos, B. Hillebrands, and E. Th. Papaioannou, Study of fully epitaxial Fe/Pt bilayers for spin pumping by ferromagnetic resonance spectroscopy, *Phys. Rev. B* **93**, 134405 (2016).
- [52] T. Valet and A. Fert, Theory of the perpendicular magnetoresistance in magnetic multilayers, *Phys. Rev. B* **48**, 7099 (1993).
- [53] Yao-Hui Zhu, Burkard Hillebrands, and Hans Christian Schneider, Signal propagation in time-dependent spin transport, *Phys. Rev. B* **78**, 054429 (2008).
- [54] Cyril Petitjean, David Luc, and Xavier Waintal, Unified Drift-Diffusion Theory for Transverse Spin Currents in Spin Valves, Domain Walls, and Other Textured Magnets, *Phys. Rev. Lett.* **109**, 117204 (2012).
- [55] S. Lepadatu, Unified treatment of spin torques using a coupled magnetisation dynamics and three-dimensional spin current solver, *Sci. Rep.* **7**, 12937 (2017).
- [56] J Rychły, J. W. Kłos, and M Krawczyk, Spin wave damping in periodic and quasiperiodic magnonic structures, *J. Phys. D: Appl. Phys.* **49**, 175001 (2016).
- [57] Justin M. Shaw, Hans T. Nembach, T. J. Silva, and Carl T. Boone, Precise determination of the spectroscopic g-factor by use of broadband ferromagnetic resonance spectroscopy, *J. Appl. Phys.* **114**, 243906 (2013).
- [58] J. Bland and B. Heinrich, *Ultrathin Magnetic Structures IV: Applications of Nanomagnetism* (Springer, Heidelberg, 2005).
- [59] J. Brandão, S. Azzawi, A. T. Hindmarch, and D. Atkinson, Understanding the role of damping and Dzyaloshinskii-Moriya interaction on dynamic domain wall behaviour in platinum-ferromagnet nanowires, *Sci. Rep.* **7**, 4569 (2017).
- [60] J. Foros, G. Woltersdorf, B. Heinrich, and A. Brataas, Scattering of spin current injected in Pd(001), *J. Appl. Phys.* **97**, 10A714 (2005).
- [61] H. Głowiński, A. Żywczak, J. Wrona, A. Krysztofik, I. Gościańska, T. Stobiecki, and J. Dubowik, CoFeB/MgO/CoFeB structures with orthogonal easy axes: Perpendicular anisotropy and damping, *J. Phys.: Condens. Matter* **29**, 485803 (2017).
- [62] Yi Liu, Zhe Yuan, R. J. H. Wesseling, Anton A. Starikov, and Paul J. Kelly, Interface Enhancement of Gilbert Damping from First Principles, *Phys. Rev. Lett.* **113**, 207202 (2014).
- [63] A. Conca, B. Heinz, M. R. Schweizer, S. Keller, E. Th. Papaioannou, and B. Hillebrands, Lack of correlation between the spin-mixing conductance and the inverse spin Hall effect generated voltages in CoFeB/Pt and CoFeB/Ta bilayers, *Phys. Rev. B* **95**, 174426 (2017).
- [64] J. C. A. Huang, T. E. Wang, C. C. Yu, Y. M. Hu, P. B. Lee, and M. S. Yang, Epitaxial growth and characterization of (100) and (110) permalloy films, *J. Cryst. Growth.* **171**, 442 (1997).
- [65] S. O. Valenzuela, in *Spin Current*, edited by S. Maekawa, S. O. Valenzuela, E. Saitoh, and T. Kimura (Oxford University Press, Oxford, 2012).